

4π Compton imaging with single 3D position sensitive CdZnTe detector

Dan Xu^{*}, Zhong He, Carolyn E. Lehner, Feng Zhang

Department of Nuclear Engineering and Radiological Sciences, University of Michigan, 2355
Bonisteel Blvd., Ann Arbor, MI 48109-2104, USA

ABSTRACT

A 3D CdZnTe detector can provide 3D position information as well as energy information of each individual interaction when a gamma ray is scattered or absorbed in the detector. This unique feature provides the 3D CdZnTe detector the capability to do Compton imaging with a single detector. After detector calibration, real-time data acquisition and imaging are implemented with a single detector system. Because the detector has a finite size and any point in the detector can be the first scattering position, 3D gamma-ray imaging in near field is possible. In this work we will show the result of the 4π Compton imaging with a single $15\text{mm} \times 15\text{mm} \times 10\text{mm}$ CdZnTe detector. Different algorithms for sequence and imaging reconstruction will be addressed and compared. The angular uncertainty is estimated and the most recent results from measurements are presented.

Keywords: Compton Imaging, 3D CdZnTe detector, near field imaging, maximum likelihood, filtered back-projection

I. INTRODUCTION

Compton camera takes advantage of the scattering kinematics if an incident photon interacts two or more times with detectors. The interaction positions will determine the direction of the photon after the first scattering, and the energy depositions will decide the first scatter angle. Therefore the source position can be limited on a cone with the vertex located at the first scattering position. For a photon without any prior knowledge about its polarization information, there is no preference for the photon to be at different positions on the cone, thus a uniform cone is reconstructed. Once many cones are obtained, various algorithms can be applied to reconstruct the true source image. Because this imaging technique eliminates the requirement of a mechanical collimator, it is sometimes also referred to as electronic collimation technique¹. Electronic collimation using Compton scattering usually has a much larger event number than mechanical collimation; however, each event obtained with electronic collimation contains less information, because the source can locate on any position on the projection cone. Furthermore, the angular resolution of mechanical collimation is mainly determined by the characteristics of the collimator; while in electronic collimation, the angular resolution can be affected by both the position and energy resolution of the detector system, and can vary from event to event. Various algorithms have been developed to overcome those difficulties. Singh proposed several reconstruction methods such as ML, EM, and ART, etc.^{2,3}. However, those algorithms usually require binning of the data which becomes impractical when the precision of the system increases. Barrett, Parra and Wilderman^{4,6} developed list-mode maximum likelihood estimation algorithm to avoid the data binning requirement. Although maximum likelihood estimation algorithms usually can provide better results, they need excessively computing resources because of their iterative characteristics. In traditional computer tomography, filtered back-projection (FBP) is a well-understood and effective algorithm in image reconstruction. However, due to the lack of fast algorithms in Fourier transform on spherical coordinates, filtered back-projection algorithm was not very successfully applied to Compton cameras until recent years⁷⁻⁹. In this paper, both maximum likelihood estimation algorithm and filtered back-projection algorithm will be examined and compared. Traditionally, Compton cameras consist of two position sensitive detectors or detector array. The front detector acts as a scatter material and the back/side detector captures the scattered photon. From the position and energy information recorded by the detector system, the cone of possible source locations is generated. This design requires the photon to be scattered in the first detector followed by an absorption in the second detector, which results very low efficiency. Furthermore, the geometry of the detector system limits the imaging solid angle. With a single 3D position sensitive detector, because the separation distance between the first and second scatter positions is small, it can achieve higher

^{*} xud@engin.umich.edu; phone 1 734 764-0338;

efficiency than two detector system by 1~2 orders of magnitude due to much larger solid angle the detector covers from the first scattering position¹⁰.

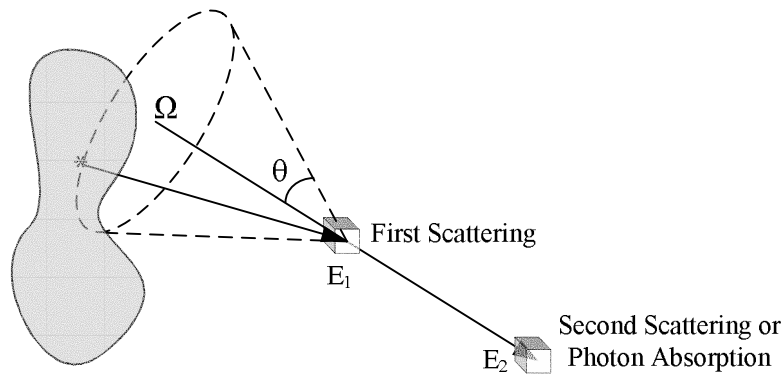


Figure 1. Cone projection of a Compton scattering event. The two interaction positions determine Ω , which is the direction of the cone axis. The energy deposited at the first scattering position and the total energy of the photon determine the half angle of the cone.

In this work, we will show the most recent progress of using a single 3-D position sensitive CdZnTe detector to do Compton imaging. The detector is 15mm×15mm×10mm in dimension and its anode is pixellated into an 11×11 array. The depth information is obtained by measuring the electron drift time from the interaction positions to the anodes. Currently, the position resolution is about 1.2mm in each direction, and energy resolution at 662keV is 1.1% and 1.6% for single and double pixel events, respectively¹¹.

Compton imaging is usually performed off-line, because it requires intensive computation, especially for iterative algorithms such as list-mode maximum likelihood method. However, simple back-projection and filtered back-projection do not need iterations and can reconstruct the image event by event. Along with the advances in computing power of personal computers, real time Compton imaging with a single 3D CdZnTe detector was achieved in this work. Furthermore, virtually any computer connected to the data acquisition computer via the internet can perform real time imaging. This will provide the possibility that a fast central computer can process data from multiple detectors placed at different locations.

Since the detector has a finite size, it is possible to do 3D imaging in near field, which will be discussed in section II. The angular uncertainty of each event must be estimated for both sequence and image reconstruction. Based on error propagation, a new method to estimate the angular uncertainty caused by detector position resolution is described in section III. By applying a single detector as the Compton imager, the sequence information which is guaranteed in two detector systems is not available. Therefore, sequence reconstruction algorithms must be developed to decide the correct order of interactions in the detector. In this paper, different algorithms of sequence reconstruction will be reviewed and compared in section IV. Finally, we will discuss different image reconstruction algorithms and their performance in section V.

II. 3D COMPTON IMAGING

The principle of Compton scattering imaging is well known. Once the positions of the first and second interactions are measured, the direction of the cone axis is determined. The half angle of the cone is decided by the energy deposited at the first scattering position and the total energy of the photon.

$$\cos \theta = 1 + \frac{m_e c^2}{E_0} - \frac{m_e c^2}{E_0 - E_1} \quad (1)$$

In a two-detector Compton imaging system, the scatter angle θ is limited to a certain range; while in a single detector Compton imaging system, the scatter angle can be any value. For simple back-projection reconstruction method, those cones are projected onto a sphere around the detector. If the radius of the sphere is large comparing with the size of the detector, the vertexes of all cones can be placed on the center of the sphere. This approximation is also referred as “far field imaging”. When the source is close enough to the detector, the size of the detector is no longer negligible. For different events, since their vertex positions are different, special consideration must be taken to correct the displacement of the vertex from the origin. This technique is also referred as “near field imaging”.

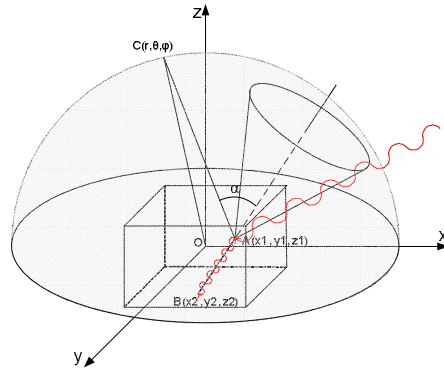


Figure 2. Near field imaging at focus distance r .

In near field imaging, the vertex of the back-projection cone should be placed at the position of the first interaction rather than at the center of the detector. As illustrated in Figure 2, point C is on the focal sphere with radius r , point A is the position of the first interaction, and the angle α between line CA and the axis of the cone is calculated and compared with the half angle of the cone to determine the value of that point.

With this simple near field imaging correction, the radius of the focal sphere must be preset. If the source is not located on the focal sphere, the image of the source is blurred. This is analogous to any optical system: the image is always the clearest on the focal plane. Figure 3 shows the images got at different focus distances for the same measurement, and Figure 4 shows the influence of focus distance on the image resolution. It is evident that when the focus distance is 37mm, which is the true source to detector distance, the reconstructed image has the best resolution.

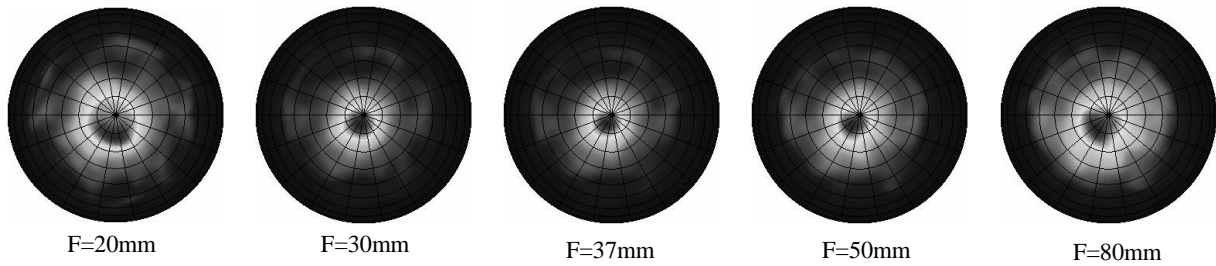


Figure 3. Reconstructed images at different focus distances. The measurement was taken with a ^{137}Cs point source placed 37mm above the detector. The reconstruction algorithm was MLEM and stopped at 6th iteration.

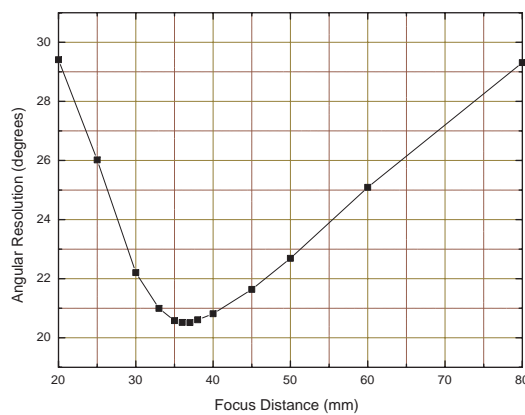


Figure 4. Image resolution versus focus distance.

Since any point in the detector can act as the vertex of a back-projection cone, it is possible to back project the cone into 3-dimensional space instead of a sphere. Therefore, 3D imaging is possible with near field imaging, although projecting the cone into 3D space need much more storage space and computing resource. The same measurement was reconstructed with 3D imaging technique, and the result is shown in Figure 5. The image indicates that a single 3D CdZnTe detector can not only do 2D imaging, it can also provide the source to detector distance. The resolution in radial direction is mostly limited by the size of the detector, which is still very small at the current stage. If the detectors can be fabricated into arrays, more powerful 3D imaging capability will be achieved.

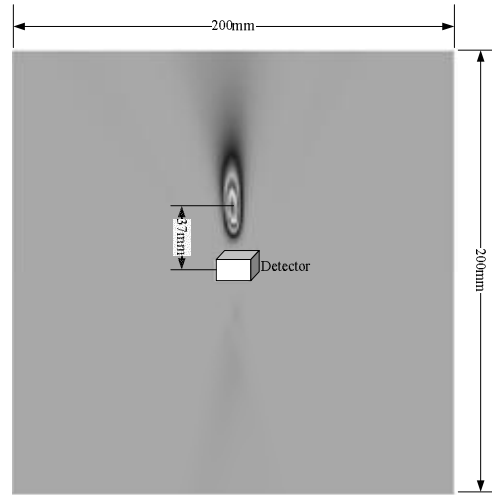


Figure 5. A vertical slice through the center of the detector in 3-D Compton imaging. The measurement was taken with a ^{137}Cs point source placed 37mm above the detector. The reconstruction algorithm was MLEM and stopped at 24th iteration.

III. ANGULAR UNCERTAINTY

For each event, the angular uncertainty is affected by both energy and position resolution of the detector system. The detector position uncertainty will cause the uncertainty of the cone axis; and the detector energy resolution will decide the uncertainty of the half angle. The angular uncertainty is important in both sequence and image reconstruction. Doppler broadening of the scatter angle is ignored because this effect is relatively small comparing with the angular resolution achievable with the current system.

The contribution from energy resolution can be calculated by means of error propagation based on Eq. 1¹⁰. Suppose there are N interactions in a single event, the angular uncertainty caused by energy resolution is

$$\left(\frac{\Delta\theta_e}{m_e c^2}\right)^2 = \frac{(E_0 - E_1)^4 (\Delta E_1)^2 + [E_1^2 + 2E_1(E_0 - E_1)]^2 \sum_{i=2}^N \Delta E_i^2}{E_0^4 (E_0 - E_1)^4 \sin^2 \theta}, \quad (2)$$

in which $m_e c^2$ is the rest mass energy of an electron, E_0 is the total energy of the incident photon, E_i is the energy deposited at ith interaction, and θ is the first scatter angle.

The position uncertainty contribution to the angular uncertainty of the back-projection cone is more complex. The position uncertainty is about 1.2mm in the lateral coordinates due to the pixellation on the detector anode surface, and 1.0mm in depth due to the uncertainty of the electron drift time measurement. In previous study, the angular uncertainty due to position resolution is calculated by simulations. The detector depth was separated into 20 bins. Therefore the whole detector volume was divided into over 2000 small voxels. For each pair of voxels, two points were randomly sampled within the two voxels and a vector was drawn between the two points. The angle between this vector and the line connecting the centers of the two voxels was then calculated¹². Many vectors were sampled for each pair of voxels and the angular uncertainty of the axis between these two voxels was then estimated.

This method is simple and straightforward. However, this method assumes that for each pair of voxels, the angular uncertainties due to position resolution are the same at all directions. This is not always true in reality, especially for two

neighboring pixels. Here we will derive the uncertainty of the cone axis in azimuthal and polar angles from error propagation, and the uncertainty at any other angle can be approximated by these two uncertainties. Suppose the first two interaction positions are $P_1(x_1, y_1, z_1)$ and $P_2(x_2, y_2, z_2)$, and the cone axis connected by these two points is at the direction of (θ, φ) . It is easy to know:

$$\varphi = \tan^{-1} \frac{y_2 - y_1}{x_2 - x_1}, \quad (3)$$

and,

$$\theta = \tan^{-1} \frac{z_2 - z_1}{\sqrt{(x_2 - x_1)^2 + (y_2 - y_1)^2}} \quad (4)$$

From error propagation, we can get:

$$\sigma_\varphi^2 = \frac{1}{(x_2 - x_1)^2 + (y_2 - y_1)^2} \cdot \frac{p^2}{6}, \quad (5)$$

and,

$$\sigma_\theta^2 = \frac{1}{[(x_2 - x_1)^2 + (y_2 - y_1)^2 + (z_2 - z_1)^2]^2} \left[(z_2 - z_1)^2 \cdot \frac{p^2}{6} + 2[(x_2 - x_1)^2 + (y_2 - y_1)^2] (\Delta z)^2 \right]. \quad (6)$$

Here, p is the pixel size of the detector, and Δz is the depth uncertainty.

However, σ_θ and σ_φ are not orthogonal on the unit sphere. We define another angular uncertainty σ_φ' , which is shown in Figure 6 to be the angular uncertainty of the axis in azimuthal direction before it's projected onto the x-y plane.

$$\sigma_\varphi' = 2 \arcsin \left(\sin \frac{\sigma_\varphi}{2} \cos \theta \right) \quad (7)$$

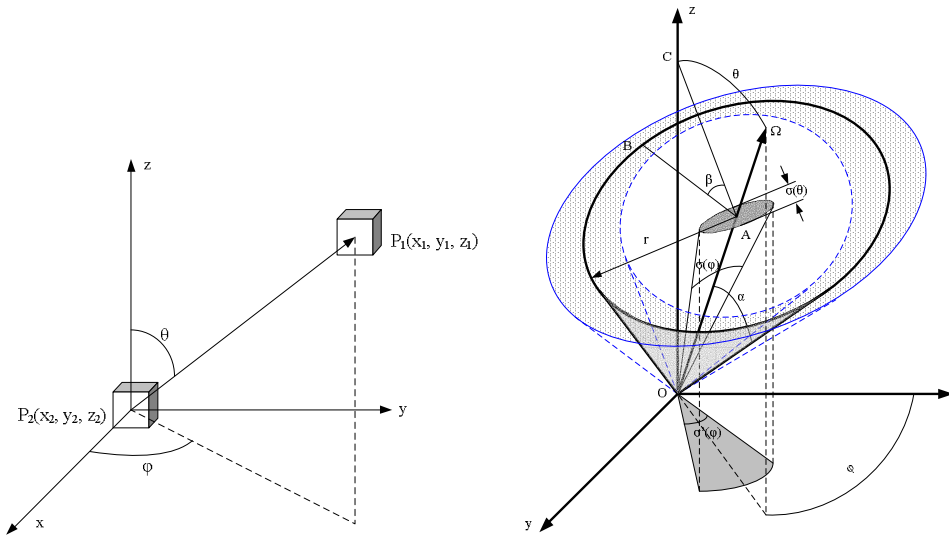


Figure 6. Angular uncertainty due to position uncertainty of the detector. In the right figure, the cone in bold lines is the back-projection cone. The axis has uncertainties in both azimuthal and polar angles, so that the back-projection cone is spread around into the shadowed ring shape area.

Since the cone axis has difference uncertainty at different directions, the cone spread will differ with angle β between line AB and plane OAC , which represents different positions on the back-projection cone. The spread of the back-projection cone at any angle β is approximated in the following way:

$$\sigma_p(\beta) = \sigma_\theta \cos^2 \beta + \sigma_\varphi \sin^2 \beta \quad (8)$$

Combined with the angular uncertainty contributed by energy resolution, the overall angular uncertainty is

$$\sigma(\beta) = \sqrt{\sigma_e^2 + (\sigma_\theta \cos^2 \beta + \sigma_\varphi \sin^2 \beta)^2} \quad (9)$$

We compared this angular uncertainty estimation algorithm with simulations, and found this method is a good approximation when the uncertainty of the cone axis differs at different angles. This helps to improve the overall image resolution. There is some distortion because of the rough approximation in Eq. (8), but it is only noticeable when the two interaction points are very close to each other or the scatter angle is very small. In reality, those events usually have poor angular resolution and are not very helpful to image reconstruction. The drawback of this algorithm is that it needs to calculate β for each pixel in one event, therefore costs more computation time.

IV. SEQUENCE RECONSTRUCTION

In a two-detector Compton imaging system, the interaction sequence is known a priori. However, in a single 3D CdZnTe detector, the timing resolution is much larger than the flight time of a photon between interactions. The sequence of interactions must be reconstructed from the energy or position information of the event.

1. Two Interactions

For two interactions, previous study used a simple method by comparing the two energy depositions. Geant4 simulations indicate that in a 15mm×15mm×10mm CdZnTe detector, when the incident photon energy is greater than 400keV, the interaction with higher energy deposition has more chance to be the first interaction, and vice versa. So the sequence reconstruction algorithm for two pixel events is simply to choose the higher energy deposition to be the first interaction for gamma rays with energy higher than 400keV, and for gamma rays with energy lower than 400keV, the algorithm chooses the lower energy deposition to be the first interaction.

However, for gamma rays with energy greater than 400keV, this algorithm will sometimes give a sequence which is physically impossible. For example, a photon can deposit very small amount of energy during the first scattering, and the energy of the scattered photon is beyond the Compton edge. If the scattered photon is absorbed by the detector by photoelectric absorption, the sequence reconstruction algorithm by simple comparison will give the wrong sequence, which is physically impossible. This situation can be avoided by doing a Compton edge test first. If one of the two energy depositions is beyond the Compton edge, the other interaction will be chosen as the first interaction.

From Geant4 simulations, this simple comparison algorithm for sequence reconstruction can correctly identify 58% of sequences at 662keV with full energy depositions. Considering at this energy, about 20% events will deposit more than 1 interaction under a same pixel, and those events are regarded as “unreconstructable” events, 58% is a reasonable percentage. Studies also show that for those events with 2 or more interactions under the same pixel, the sequence got by the simple comparison algorithm can still contribute to image the correct source location.

Another sequence reconstruction algorithm is deterministic algorithm based on Klein-Nishina formula:

$$\frac{d\sigma_c}{d\Omega} \propto \left[\frac{1}{1 + \alpha(1 - \cos\theta)} \right]^2 \left(\frac{1 + \cos^2\theta}{2} \right) \left[1 + \frac{\alpha^2(1 - \cos\theta)^2}{(1 + \cos^2\theta)[1 + \alpha(1 - \cos\theta)]} \right], \quad (10)$$

in which $\alpha = hv/m_e c^2$. The probability density function of a photon to be scattered at angle θ then is:

$$\Sigma(\theta) \propto \int_0^{2\pi} \frac{d\sigma_c}{d\Omega} \sin\theta d\varphi \propto 2\pi \left[\frac{1}{1 + \alpha(1 - \cos\theta)} \right]^2 \left(\frac{1 + \cos^2\theta}{2} \right) \left[1 + \frac{\alpha^2(1 - \cos\theta)^2}{(1 + \cos^2\theta)[1 + \alpha(1 - \cos\theta)]} \right] \sin\theta \quad (11)$$

For a two-pixel event, there are two possible sequences, which correspond to two different scatter angles.

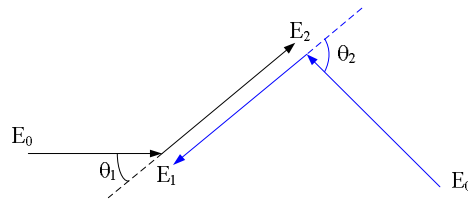


Figure 7. Two possible sequences in a two-pixel event. θ_1 and θ_2 are the two possible scatter angles.

To decide which sequence has more probability, we assume there is a small energy perturbation dE in the first interaction. Since the total energy E_0 is constant, the change in E_2 then is $-dE$. From Eq. (1),

$$d\theta_1 = \frac{m_e c^2}{\sin \theta_1 E_2^2} dE_2 = -\frac{m_e c^2}{\sin \theta_1 E_2^2} dE \quad (12)$$

So, the probability for a photon with energy E_0 to leave an energy deposition between E_1 and E_1+dE in the first interaction is $\Sigma(\theta_1)d\theta_1$. Therefore, in the deterministic sequence reconstruction algorithm for two-pixel events, the figure of merit is defined as:

$$FOM_1 = \frac{\Sigma(\theta_1)}{\sin \theta_1 E_2^2} \propto 2\pi \left[\frac{1}{1 + \alpha(1 - \cos \theta_1)} \right]^2 \left(\frac{1 + \cos^2 \theta_1}{2} \right) \left[1 + \frac{\alpha^2 (1 - \cos \theta_1)^2}{(1 + \cos^2 \theta_1)[1 + \alpha(1 - \cos \theta_1)]} \right] \frac{1}{E_2^2} \quad (13)$$

The deterministic sequence reconstruction algorithm has close performance comparing with the simple comparison method, except that deterministic algorithm is about 15% better at medium energy around 500keV.

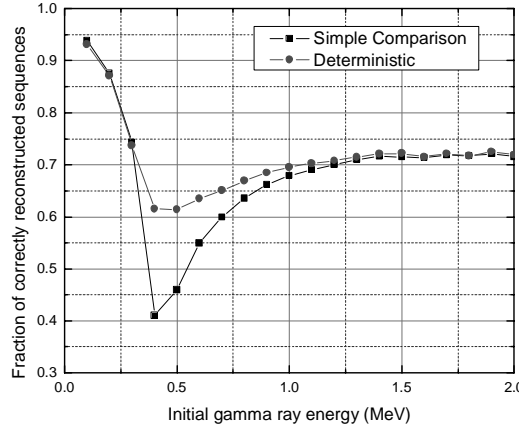


Figure 8. Fraction of simulated correctly reconstructed sequences by simple comparison and deterministic sequence reconstruction algorithms.

2. Three Interactions

Sequence reconstruction for three-pixel events is more complicated. Current techniques include “backtracking”¹³, deterministic method¹⁴, and “chi-squared” or “minimum squared difference” (MSD) method^{10, 15, 16}. Here we will only discuss the last two algorithms.

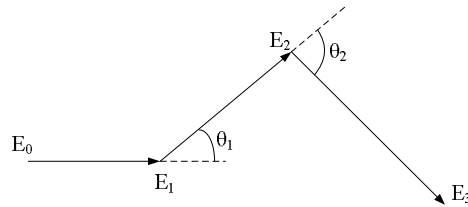


Figure 9. Three interactions. The second scatter angle can be calculated from both energy and position information.

MSD method compares the cosines of the second scatter angle calculated from energy and position information, and defines the figure of merit by dividing the square of their difference by the uncertainty in that difference:

$$FOM_{MSD} = \frac{(\cos \theta_{2e} - \cos \theta_{2r})^2}{\sigma^2 (\cos \theta_{2e} - \cos \theta_{2r})} = \frac{(\cos \theta_{2e} - \cos \theta_{2r})^2}{\sin^2 \theta_{2e} \sigma^2 (\theta_{2e}) + \sin^2 \theta_{2r} \sigma^2 (\theta_{2r})} \quad (14)$$

From error propagation, the uncertainty in θ_{2e} and θ_{2r} can be calculated as:

$$\sigma^2 (\theta_{2e}) = \frac{(m_e c^2)^2}{\sin^2 \theta_{2e}} \left[\frac{1}{(E_2 + E_3)^4} \sigma_{E_2}^2 + \frac{(2E_3 + E_2)^2 E_2^2}{(E_2 + E_3)^4 E_3^4} \sigma_{E_3}^2 \right], \quad (15)$$

and

$$\sigma^2(\theta_{2r}) = \frac{2\sigma^2 [r_{12}^2 + r_{23}^2 + r_{12}r_{23} \cos \theta_{2r}]}{r_{12}^2 r_{23}^2} \quad (16)$$

In Eq. (16), we made an assumption of $\sigma_x^2 = \sigma_y^2 = \sigma_z^2 = \sigma^2$ to simplify the expression.

The deterministic algorithm for three-pixel events is similar to the algorithm for two-pixel events. The figure of merit is defined as:

$$FOM_{Deterministic} = \Sigma(\theta_1 | E_1 + E_2 + E_3) \cdot \frac{1}{\sin \theta_1 (E_2 + E_3)^2} \cdot \Sigma(\theta_2 | E_2 + E_3) \cdot \frac{1}{\sin \theta_2 E_3^2}, \quad (17)$$

where $\Sigma(\theta|E)$ stands for the cross section of a photon with energy E to be scattered at angle θ .

The performances of the two algorithms are very close.

Table 1. Fraction of correctly reconstructed sequences at 662keV by MSD and deterministic sequence reconstruction algorithms. Events with multiple interactions under a same pixel are always regarded as incorrectly reconstructed, although they still contribute to the imaging.

	All Events	Full Energy Deposit
MSD	44.2%	52.1%
Deterministic	43.9%	51.8%

However, the first scatter angle distribution of correctly reconstructed events shows that MSD algorithm tends to correctly identify those events with smaller scatter angles, which have better angular resolution. Therefore, although the fraction of correctly reconstructed events by deterministic algorithm is very close to MSD algorithm, MSD algorithm is used in this work.

V. IMAGE RECONSTRUCTION

The simplest way to reconstruct a Compton image is to back project the cones to the imaging plane or sphere. This is sometimes called “event circle” method. Here we will refer it as “simple back-projection” algorithm, to correspond to the “filtered back-projection” algorithm which is also studied in this paper. Another popular algorithm in Compton image reconstruction is maximum likelihood estimation via the expectation maximum algorithm (MLEM).

1. Simple back-projection

Simple back-projection method is the most straight forward algorithm. Since each event provides the information of the possible source locations which are uniformly distributed on a cone, those cones are simply summed up together. Because theoretically every cone will pass the true source location, the source can then be enhanced and be distinguished from the background.

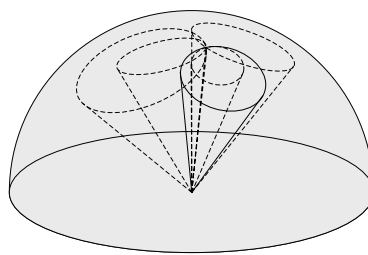


Figure 10. Simple back-projection algorithm sums all cones on the imaging sphere to form the image.

The image reconstructed by simple back-projection algorithm is usually blurred because the cones overlap with each other. Currently the angular resolution achieved by simple back-projection algorithm is about 50 degrees. However, since this method is simple and fast, it might be useful in some applications that require fast response rather than good angular resolution, such as source probing.

2. Filtered back-projection

Even with perfect detector performance, i.e., perfect energy and position resolution, and correct sequence, the simple back-projection still suffers from the random distribution of cone axis directions. Parra⁸ proposed FBP algorithm to deconvolute the blurring in spherical harmonics domain. With perfect detector performance, a point source will generate a simple back-projection image as:

$$h_{bp}(\cos \omega_0) = \frac{1}{\sqrt{1 - \cos^2 \frac{\omega_0}{2}}} \int_{-\cos^2 \frac{\omega_0}{2}}^{\cos^2 \frac{\omega_0}{2}} dz \frac{h(z)}{\sqrt{\cos^2 \frac{\omega_0}{2} - z^2}}, \quad (18)$$

in which ω_0 is the angle between the image pixel direction and the source direction, and $h(z)$ is defined by Klein-Nishina formula:

$$h(\cos \omega) = h_c(\cos \omega) = \frac{1 + \cos^2 \omega + \frac{\gamma^2 (1 - \cos \omega)^2}{1 + \gamma(1 - \cos \omega)}}{(1 + \gamma(1 - \cos \omega))^2} \quad (19)$$

Surprisingly the above integral has a closed form:

$$h_{bp}(\cos \omega_0) = \frac{\pi}{\gamma^2 \sqrt{1 - k^2}} \left\{ \frac{\left[2\gamma^4(\gamma^2 - 2\gamma - 2)k^4 + \gamma^2(-4\gamma^4 + 17\gamma^2 + 18\gamma + 6)k^2 + 2(\gamma + 1)^2(\gamma^4 - 2\gamma^2 - 3\gamma - 1) \right] + 1}{2 \left[(1 + \gamma)^2 - \gamma^2 k^2 \right]^{\frac{5}{2}}} \right\}, \quad (20)$$

where $k = \cos \frac{\omega_0}{2}$, and γ is the ratio of the initial gamma ray energy and rest mass of an electron.

Eq. (18) or (20) is the point spread function (PSF) of the system. Suppose the simple back-projection generates an image of $g'(\Omega)$, then FBP algorithm will deconvolute the PSF out of $g'(\Omega)$ to form the filtered image of $g(\Omega)$. The deconvolution can actually be performed through a convolution:

$$g(\Omega) = \int d\Omega' g'(\Omega') h^{-1}(\cos \omega), \quad (21)$$

in which:

$$h^{-1}(\cos \omega) = \sum_{n=0}^{\infty} \left(\frac{2n+1}{4\pi} \right)^2 \frac{P_n(\cos \omega)}{H_n}. \quad (22)$$

In the above equations, ω is the angle between Ω and Ω' , and H_n are the coefficients of $h_{bp}(\cos \omega)$ expanded on Legendre polynomials.

$$H_n = \frac{2n+1}{2} \int d(\cos \omega) h_{bp}(\cos \omega) P_n(\cos \omega) \quad (23)$$

Fortunately, H_n converge to a constant value rather than zero when n is large, thus avoid the instability problem usually faced by deconvolution process. If PSF other than Eq. (20) will be used, and H_n vanish to zero when n is large, the image must be low pass filtered before deconvolution.

Convolution of Eq. (21) can be performed either in angular space or by transforming into spherical harmonics space, filtering, and then transforming back into angular space. Parra also suggested an “event response function” method to combine the back-projection and filtering into a single filtered back-projection step. However, due to recent progresses in fast algorithms of Fourier transform on spherical coordinates¹⁷⁻¹⁹, it is possible to perform the convolution of Eq. (21) directly. Since FBP algorithm can also be performed event by event, it is easy to implement this algorithm in real time imaging. The computation cost of FBP is only slightly more than simple back-projection algorithm, but it can achieve much better angular resolution. Currently, detector errors are not taken into consideration. If detector errors are considered, there is still room for further improvement.

3. List-mode MLEM

MLEM is an iterative algorithm that will converge to a source distribution having the maximum likelihood for the measured data set to be observed. The convergence is assured if the total number of events is greater than the pixel number in the image. The iteration is performed by the following equation^{6, 20}:

$$\lambda_j^{n+1} = \frac{\lambda_j^n}{s_j} \sum_i \frac{Y_i t_{ij}}{\sum_k t_{ik} \lambda_k^n}, \quad (24)$$

in which λ_j^n is the estimated value of pixel j at n^{th} iteration, s_j is the probability of an emission from pixel j to be detected, Y_i is the number of times that measurement i is observed, $i=\{1,2,\dots,i,\dots,I-1,I\}$ includes all possible measurement outputs, and t_{ij} is the probability of an emission from pixel j to be observed as measurement i . The matrix t_{ij} is also called the system model or matrix. Iterations can be terminated by some preset stopping criterion. However, in practice, computation time usually sets the limit to terminate the iterations early. The system matrix can be modeled analytically:

$$t_{ij} = \exp(-\sigma_t(E_0)r_{01}) \frac{d\sigma_c}{d\Omega} \exp(-\sigma_t(E')r_{12}) \quad (25)$$

where $\sigma_t(E)$ is the total absorption cross section for a photon at energy E , E_0 and E' are the initial and scattered photon energies, respectively, r_{01} is the attenuation distance between the source pixel and the first interaction, r_{12} is the attenuation distance between the first and second interactions, and $d\sigma_c/d\Omega$ is differential Compton cross section, which is approximated by the Klein-Nishina cross section (10) divided by r_{12}^2 . Therefore, the system matrix is the product of the probabilities for the initial gamma ray to reach the first interaction point, be scattered at angle θ , and for the scattered photon to reach the second interaction location.

The number of the possible measurement outputs can be very large. For an N -pixel event, the measurement output is a $4N$ dimensional vector, including $3N$ dimensions in positions and N dimensions in energy. Therefore, the system matrix could be extremely large to keep the information loss low. List mode maximum likelihood was introduced to overcome this difficulty by setting $Y_i=I$ for all measured events and zero for all unmeasured events. This assumption is usually valid because the chance for two measurements to be exactly the same is extremely low. Therefore, the summation over all possible measurement outputs in Eq. (24) becomes a summation over all measured events. By this way the system matrix t_{ij} can be calculated on the fly and thus eliminates the requirement to pre-calculate and store the system matrix.

When reconstructing an event, the system matrix is only calculated on the back projection cone and set to zero elsewhere, because if the source pixel is not on that cone, it is obvious that there is no chance for a photon with energy E_0 to be detected as the measured event. We also found that the last two terms in the system matrix model of Eq. (25), $d\sigma_c/d\Omega$ and $\exp(-\sigma_t(E')r_{12})$, are independent on the locations of source pixels. Noticing that in Eq. (24), there are system matrices on both numerator and denominator, these two terms will eventually cancel with each other. The first term, $\exp(-\sigma_t(E_0)r_{01})$, is the source pixel position determined, because r_{01} depends on the source pixel position, and is a quite complicated function. However, for small detector system such as a 15mm×15mm×10mm 3D CdZnTe detector, we found the ratio of the maximum value of this term to its minimum value is very close to 1, which indicates this term in the system matrix model can also be considered as constant.

Therefore, as long as the detector is small enough, t_{ij} is almost constant for all the pixels on the back-projection cone. In Eq. (24), t_{ij} will eventually be normalized, so it is equivalent to replace all t_{ij} with 1. By this way, the calculation of the system matrix can be skipped, and great amount of computation cost is then saved. After this approximation, the MLEM algorithm in one iteration cycle almost has the same speed as the simple back-projection algorithm, while the image almost has no noticeable difference from the image reconstructed with the original system matrix.

4. Performance

Due to the asymmetry in the detector system, the angular resolutions are different in azimuthal and lateral directions. Currently, the angular resolutions achieved by different reconstruction algorithms are listed in Table 2.

Table 2. Angular resolution (FWHM) achieved by different image reconstruction algorithms.

	Simple back-projection	FBP	MLEM (24 iterations)
FWHM in azimuthal direction (degrees)	47.7	19.1	10.1
FWHM in lateral direction (degrees)	61.4	29.6	14.4

Only full energy events were imaged by those reconstructions. To verify the above resolution, two point ^{137}Cs sources of nearly equal activity were placed 15 degrees apart at the side of the detector. Surprisingly, the two sources are still resolvable even with 19.1 degrees angular resolution in FBP. Since FBP algorithm does not need iterations and its speed is comparable with simple back-projection algorithm, it can be used as a start point of MLEM algorithm thus decreases the iteration times. Currently, FBP algorithm is equivalent to MLEM at about 5th iteration.

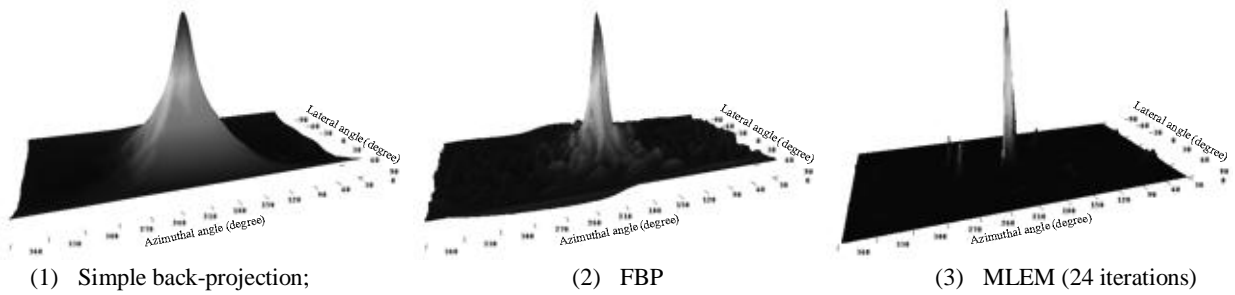


Figure 11. A point ^{137}Cs source images reconstructed by simple back-projection, FBP and MLEM, respectively.

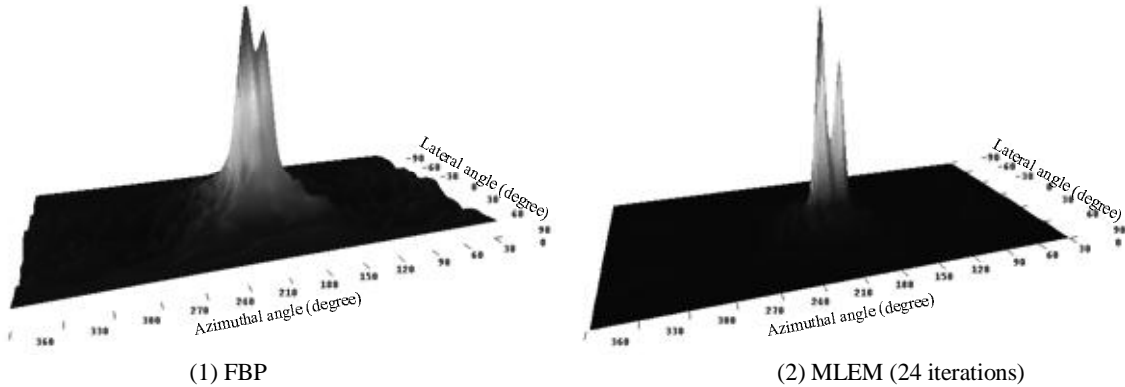


Figure 12. Images of two point ^{137}Cs sources placed 15° apart by FBP and MLEM separately

VI. CONCLUSIONS

A single 3D CdZnTe detector is proven to be capable of doing 4π Compton imaging. When the detector size increases, it is also able to do 3D imaging. Real-time data acquisition and imaging were implemented with simple back-projection and FBP reconstruction algorithms. With a single $15\text{mm}\times 15\text{mm}\times 10\text{mm}$ 3D CdZnTe detector and currently available ASICs, an angular resolution of 10° at 662keV was achieved by list-mode MLEM reconstruction algorithm after 24 iterations. Filtered back-projection is a promising algorithm since it is fast and does not need iteration. Current achieved angular resolution by FBP is about 19° at 662keV, and there is still room for further improvement if detector error is taken into consideration.

REFERENCES

1. R. R. Brechner and M. Singh, "Iterative reconstruction of electronically collimated SPECT images," *Nuclear Science, IEEE Transactions on*, vol. 37, pp. 1328-1332, 1990.
2. M. Singh, "An electronically collimated gamma camera for single photon emission computed tomography. Part I: Theoretical considerations and design criteria," *Medical Physics*, vol. 10, pp. 421-427, 1983.
3. R. L. Tom Hebert, Manbir Singh, "Three-dimensional maximum-likelihood reconstruction for an electronically collimated single-photon-emission imaging system," *Optical Society of America*, vol. 7, pp. 1305-1313, 1990.
4. H. H. Barrett, et al., "List-mode likelihood," *Journal of the Optical Society of America A (Optics, Image Science and Vision)*, vol. 14, pp. 2914-23, 1997.
5. L. Parra and H. H. Barrett, "List-mode likelihood: EM algorithm and image quality estimation demonstrated on 2-D PET," *IEEE Transactions on Medical Imaging*, vol. 17, pp. 228-35, 1998.
6. S. J. Wilderman, N.H. Clinthorne, J.A. Fessler, W.L. Rogers, "List-mode likelihood reconstruction of Compton scatter camera images in nuclear medicine," *Proceedings of the 1998 IEEE Nuclear Science Symposium*, vol. 3, pp. 1716-1720, 1998.

7. M. J. Cree and P. J. Bones, "Towards direct reconstruction from a gamma camera based on Compton scattering," *IEEE Transactions on Medical Imaging*, vol. 13, pp. 398-407, 1994.
8. L. C. Parra, "Reconstruction of cone-beam projections from Compton scattered data," *Nuclear Science, IEEE Transactions on*, vol. 47, pp. 1543-1550, 2000.
9. R. Basko, et al., "Application of spherical harmonics to image reconstruction for the Compton camera," *Physics in Medicine and Biology*, vol. 43, pp. 887-894, 1998.
10. C. E. Lehner, Z. He, Z. Feng, "4-pi Compton imaging using a 3-D position-sensitive CdZnTe detector via weighted list-mode maximum likelihood," *presented at the 13th International Workshop on Room-Temperature Semiconductor X- and Gamma-Ray Detectors, IEEE Nuclear Science Symposium, Portland, Oregon, 2003.*
11. F. Zhang, Z. He, G.F. Knoll, D.K. Wehe, J.E. Berry, and D. Xu, "Improved resolution for 3-D position-sensitive CdZnTe spectrometers," *presented at the 13th International Workshop on Room-Temperature Semiconductor X- and Gamma-Ray Detectors, IEEE Nuclear Science Symposium, Portland, Oregon, 2003.*
12. C. E. Lehner, "4-Pi Compton imaging using a single 3-D position-sensitive CdZnTe detector," *Ph. D. Thesis, University of Michigan, 2004.*
13. J. van der Marel, and B.Cederwall, "Backtracking as a way to reconstruct Compton scattered gamma-rays," *Nuclear Instruments and Methods in Physics Research*, vol. A437, pp. 538-551, 1999.
14. R. A. Kroeger, W.N. Johnson, J.D. Kurfess, B.F. Philips, and E.A.Wulf, "Three-Compton telescope: Theory, simulations, and performance," *IEEE Transactions on Nuclear Science*, vol. 49, pp. 1887-1892, 2002.
15. I. Y. Lee, "Gamma-ray tracking detectors," *Nuclear Instruments and Methods in Physics Research*, vol. A422, pp. 195-200, 1999.
16. U. G. Oberlack, E. Aprile, A. Curioni, V. Egorov, K.L.Giboni, "Compton scattering sequence reconstruction algorithm for the liquid xenon gamma-ray imaging telescope (LXeGRIT)," *SPIE Proceedings*, vol. 4141, pp. 168-177, 2000.
17. J. D.M.Healy, D.N.Rockmore, P.J.Kostelec, S.Moore, "FFTs for the 2-Sphere-Improvements and Variations," *the Journal of Fourier Analysis and Applications*, vol. 9, pp. 341-385, 2003.
18. Driscoll J. R. and Healy D. M., "Computing Fourier Transforms and Convolutions on the 2-Sphere," *Advances in Applied Mathematics*, vol. 15, pp. 202-250, 1994.
19. S. Kunis and D. Potts, "Fast spherical Fourier algorithms," *Journal of Computational and Applied Mathematics*, vol. 161, pp. 75-98, 2003.
20. L. Shepp, Y. Vardi, "Maximum likelihood reconstruction for emission tomography," *IEEE Transactions on Medical Imaging*, vol. MI-1, pp. 113-122, 1982.